

Rise and fall of plaquette order in Shastry-Sutherland magnet revealed by pseudo-fermion functional renormalization group

Ahmet Keleş^{1,*} and Erhai Zhao²

¹*Department of Physics, Middle East Technical University, Ankara 06800, Turkey*

²*Department of Physics and Astronomy, George Mason University, Fairfax, Virginia 22030, USA*

The Shastry-Sutherland model as a canonical example of frustrated magnetism has been extensively studied. The conventional wisdom has been that the transition from the plaquette valence bond order to the Neel order is direct and potentially realizes a deconfined quantum critical point beyond the Ginzburg-Landau paradigm. This scenario however was challenged recently by improved numerics from density matrix renormalization group which offers evidence for a narrow gapless spin liquid between the two phases. Prompted by this controversy and to shed light on this intricate parameter regime from a fresh perspective, we report high-resolution functional renormalization group analysis of the generalized Shastry-Sutherland model. The flows of over 50 million running couplings provide a detailed picture for the evolution of spin correlations as the frequency/energy scale is dialed from the ultraviolet to the infrared to yield the zero temperature phase diagram. The singlet dimer phase emerges as a fixed point, the Neel order is characterized by divergence in the vertex function, while the transition into and out of the plaquette order is accompanied by pronounced peaks in the plaquette susceptibility. The plaquette order is suppressed before the onset of the Neel order, lending evidence for a finite spin liquid region for $J_1/J_2 \in (0.77, 0.82)$, where the flow is continuous without any indication of divergence.

Forty years after the introduction of the Shastry-Sutherland (SS) model [1], its ground state phase diagram remains inconclusive. The model describes quantum spins on the square lattice with competing antiferromagnetic exchange interactions, J_1 for the horizontal/vertical bonds and J_2 for the decimated diagonal bonds connecting the empty plaquettes, see Fig. 1. Owing to the frustration, the model has long been suspected to host exotic ground states and phase transitions. A large body of theoretical works have established the existence of three phases, see e.g. [2] and [3, 4] for a synopsis of earlier and recent results, respectively. The $J_1 < J_2/2$ limit is exactly solvable and the ground state is a product state of diagonal dimers (spin singlets). For intermediate value of J_1/J_2 , the ground state is a plaquette valence bond solid, while Neel order takes over for large J_1/J_2 . The most interesting, and controversial, question regards the nature of the plaquette-to-Neel (pN) transition: is it conventional, a deconfined quantum critical point, or through an additional spin liquid phase?

Remarkably, the SS model has an almost ideal realization in $\text{SrCu}_2(\text{BO}_3)_2$ crystals, where phase transitions can be induced by tuning the hydrostatic pressure [5, 6]. Inelastic neutron scattering found signatures of the plaquette phase [7], and heat capacity measurements confirmed the dimer-to-plaquette transition [8, 9]. Yet a direct plaquette-to-Neel transition was not observed in the anticipated pressure range. These experiments renewed the effort to examine this intriguing region using the state-of-the-art numerical techniques. Earlier tensor network (iPEPS) calculations confirmed the plaquette phase within the region $J_1/J_2 \in [0.675, 0.765]$ [10–14] and a weak first order pN transition. A recent density matrix renormalization group (DMRG) study [3] with cylinders of circumference up to ten sites yielded similar phase boundary $J_1/J_2 \in [0.675, 0.77]$ but a continuous pN transition with spin correlations supporting a deconfined quantum critical point. Another DMRG using cylinder circumference up to 14 sites concludes that a spin liquid phase exists in the window $J_1/J_2 \in [0.79, 0.82]$ be-

tween the plaquette and the Neel phase [4]. A core difficulty in reaching a consensus is attributed to the near degeneracy of the competing orders in this region. The finite-size limitation of DMRG means that the ground state can only be inferred by extrapolation via careful finite size scaling analysis.

The size restriction prompts us to adopt an alternative approach diametrically opposed to exact diagonalization or DMRG on finite systems. The algorithm directly accesses the infrared and thermodynamic limit while treating all competing orders on equal footing without bias. It starts from the microscopic spin Hamiltonian and successively integrates out the higher frequency fluctuations with full spatial (or equivalently momentum) resolution retained at each step. The scale-dependent effective couplings and correlation functions are obtained by numerically solving the Functional Renormalization Group (FRG) flow equations [15–17]. As the frequency scale Λ slides from $J_{1,2}$ down to zero, the zero temperature phase diagram is determined. Such FRG approach to quantum spin systems, first established in 2010 [18], has yielded insights for many frustrated spin models. But its application to the SS model has not been successful, perhaps due to two reasons. First, in contrast to the Neel order, the dimer or the plaquette order cannot be inferred naively from the divergence of vertex functions, making it challenging to locate their phase boundaries. Second, as we shall show below, the pN transition region is better understood by examining a generalized model that reduces to the SS model in a particular limit.

In this work, high resolution FRG analysis of the generalized SS model is achieved by overcoming these technical barriers. To maintain sufficient momentum and frequency resolution, one must keep track of millions of running couplings at each FRG step. The calculation is made possible by migrating to the GPU platform which led to performance improvement by orders of magnitude [19, 20]. Despite being a completely different approach, the phase boundaries predicted from our FRG are remarkably close to the state-of-the-art DMRG. The

agreement further establishes FRG as an accurate technique for frustrated quantum magnetism. Most importantly, the plaquette susceptibility from FRG indicates the plaquette order terminates around $J_1/J_2 \approx 0.77$ before the onset of weak Neel order around $J_1/J_2 \approx 0.82$. It supports the existence of a spin liquid region between the plaquette and Neel phase proposed in Ref. [4]. Thus, the SS model is a strong candidate to host spin liquid, and $\text{SrCu}_2(\text{BO}_3)_2$ offers exciting opportunity to realize and probe the elusive spin liquid phase.

Model and pseudofermion FRG.— Our starting point is the generalized Shastry-Sutherland Hamiltonian [21]

$$H = \kappa J_1 \sum_{\langle i,j \rangle'} \mathbf{S}_i \cdot \mathbf{S}_j + J_1 \sum_{\langle i,j \rangle''} \mathbf{S}_i \cdot \mathbf{S}_j + J_2 \sum_{i,j \in \text{diag}} \mathbf{S}_i \cdot \mathbf{S}_j \quad (1)$$

where \mathbf{S}_i are spin one-half operators ($S = 1/2$), i, j label the sites, and $J_{1,2} > 0$ are antiferromagnetic exchange couplings. The first (second) sum is over nearest neighbors on the square lattice represented by the solid (dashed) black lines in Fig. 1(a), the last sum is over the alternating diagonal bonds indicated by the red lines. The original SS model corresponds to the limit $\kappa = 1$ [1, 2]. A small $\delta J_1 = (\kappa - 1)J_1$ acts as a source field to break the double degeneracy and favor valence bond order within the shaded plaquettes. It plays a crucial role in our analysis and facilitates the calculation of plaquette susceptibility. We will stay close to the limit $\kappa \rightarrow 1$ throughout.

To predict the phase diagram of Hamiltonian Eq. (1), FRG finds its generating functional, i.e. an effective field theory parametrized by self-energies, four-point and higher-order vertices, for each given frequency/energy scale Λ . The self-energies and vertices obey the formally exact flow equations that can be truncated and solved numerically. More specifically, the many-spin problem is first converted to an interacting fermion problem using the pseudofermion representation [18], $S_i^\mu = (1/2)\sigma_{\alpha\beta}^\mu \psi_{i\alpha}^\dagger \psi_{i\beta}$. Here σ^μ are the Pauli matrices, and $\psi_{i\beta}$ annihilates a fermion at site i with spin $\beta = \uparrow, \downarrow$ etc.. The resultant fermion Hamiltonian only has quartic interactions but no kinetic energy term (the fermions are localized and constrained at one particle per site). So the bare single-particle Green function $G_0(\omega) = 1/i\omega$ with ω being the frequency [18]. Then the flow equations for the interacting fermion problem can be solved by generalizing the expansion and truncation schemes extensively benchmarked for strongly correlated electronic materials [22, 23].

The implementation of pseudofermion FRG are well documented in the original work [18] and later improvements [24–37]. A brief outline is as follows. Starting from an ultraviolet scale $\Lambda = \Lambda_{UV} \gg J_{1,2}$ and using the bare interaction in Eq. (1) and bare Green function to set up the initial condition, the coupled integro-differential equations for the scale-dependent self-energy $\Sigma^\Lambda(\omega)$ and four-point vertex $\Gamma_{i_1 i_2}^\Lambda(\omega'_1, \omega'_2; \omega_1, \omega_2)$ are solved successively in small steps along a discretized grid of the frequency/energy scale Λ until it is reduced down to the infrared $\Lambda = \Lambda_{IR} \rightarrow 0$. During the flow, the self-energy $\Sigma^\Lambda(\omega)$ is renormalized to gain nontrivial frequency dependence as higher frequency fluctuations induce retarded interactions. But it remains site-independent, i.e. fermions hop-

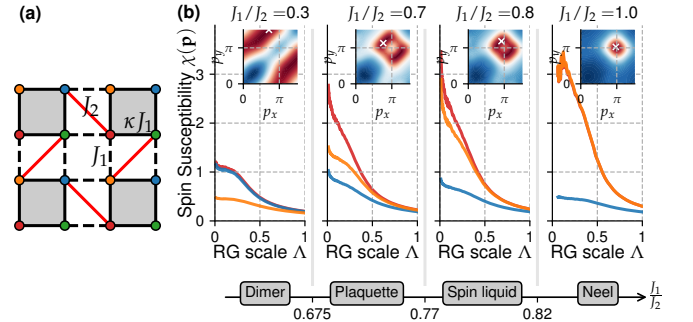


FIG. 1. Generalized Shastry-Sutherland model and its zero temperature phase diagram from FRG. (a) The competing exchange couplings in model Eq. (1) include κJ_1 and J_1 for the black solid and dashed bonds respectively, and J_2 for the red bonds. The four sites within the unit cell (shaded square) are labelled by color red, green, blue and yellow respectively. (b) The phase diagram for $\kappa = 1$ consists of four phases separated by three critical points as J_1/J_2 is varied. A representative point is chosen for each phase to illustrate the typical RG flows of the spin susceptibilities $\chi(\mathbf{p})$ in leading channels (i.e. different values of \mathbf{p} , see main text). The corresponding insets show the profile of $\tilde{\chi}_r(\mathbf{p})$ in the infrared limit $\Lambda \rightarrow 0$. The white \times indicates its peak position in the momentum space (p_x, p_y).

ping is prohibited. The four-point vertices Γ^Λ (effective interactions) carry multiple indices: i_1 and i_2 for lattice sites whereas ω'_1, ω'_2 and ω_1, ω_2 are frequencies for the pair of sites before and after the interaction. Contributions from higher order vertices are approximated by the Katanin term [38].

Care must be exercised to efficiently parametrize the vertices in order to render the numerical task tractable. In particular, the SS model has non-symmorphic lattice symmetry, with four sites per unit cell shown in colors $\alpha = r, g, b, y$ in Fig. 1 and no C_4 symmetry as in the J_1 - J_2 model. To avoid using color indices in $\Gamma_{i_1 i_2}^\Lambda$, we pick a $\alpha = r$ site located at the origin as i_1 . Other vertices for sites of different color $\alpha = g, b, y$ can be obtained from the central r -site with appropriate rotation and lattice translation [39]. We retain all i_2 within a radius $|\mathbf{r}_{i_1} - \mathbf{r}_{i_2}| < R_{\max}$ in $\Gamma_{i_1 i_2}^\Lambda$ and emphasize that the FRG equations describe infinite systems without a boundary. Here R_{\max} merely places an upper cutoff for the correlations retained in the numerics. As to the frequency variables, we rewrite $\Gamma^\Lambda(\omega'_1, \omega'_2; \omega_1, \omega_2)$ as functions of the Mandelstam variables s, t and u [18] which manifestly enforce the frequency conservation. Finally, we discretize the frequency using a logarithmic mesh of N_ω points extending from the ultraviolet scale $\Lambda_{UV} = 10^2 J_2$ to the infrared scale $\Lambda_{IR} = 10^{-2} J_2$. Typically, $N_\omega = 48$ provides good frequency resolution, and further increasing N_ω will not alter the results appreciably. We take $R_{\max} = 10$ which amounts to $N_L = 441$ lattice sites within the correlation radius. In total, this gives a coupled system of $N_L \times N_\omega^3 \sim 50$ million running couplings.

Correlation functions and susceptibilities.— To detect the emergence of long range order as $\Lambda \rightarrow 0$, correlation functions at each renormalization scale can be obtained from the Σ^Λ and Γ^Λ via standard calculations involving Feynman di-

agrams. For example, the spin-spin correlation function is given by

$$\begin{aligned}\chi_{ij}(\omega) &= \int_0^\infty d\tau e^{i\omega\tau} \langle T S_i^z(\tau) S_j^z(0) \rangle \\ &= S_i^z \text{---} S_j^z + S_j^z \text{---} S_i^z, \quad (2)\end{aligned}$$

where black dots represent the spin matrix $S_i^z = \sigma^z/2$, filled square represents vertex Γ^Λ and lines with arrows are dressed Green functions that contain the self-energy. The scale dependence of χ is suppressed for brevity. We find that it is necessary to distinguish the flows of spin correlations for different bonds, i.e. pairs of (i, j) , because the symmetry breaking patterns in the SS model are rather complex and involving valence bond orders. For a given site i of color α , one can find $\tilde{\chi}_\alpha(\mathbf{p})$, the Fourier transform of Eq. (2) in the limit of $\omega \rightarrow 0$. It is also convenient to define spin susceptibility

$$\chi(\mathbf{p}) = \lim_{\omega \rightarrow 0} \frac{1}{4} \sum_\alpha \sum_j e^{i\mathbf{p} \cdot (\mathbf{r}_\alpha - \mathbf{r}_j)} \chi_{ij}(\omega) = \frac{1}{4} \sum_\alpha \tilde{\chi}_\alpha(\mathbf{p}), \quad (3)$$

where the α sum is over the four sites of different colors within the unit cell, the j sum is over all sites, and the limit $\omega \rightarrow 0$ is taken in the end. The spin susceptibility defined in Eq. (3) has no bond resolution, but its divergence (or lack thereof) and its profile in momentum space offer a quick diagnosis of the incipient orders as the ratio J_1/J_2 is changed. Finally, we define a set of plaquette susceptibilities to detect the plaquette valence bond order. They measure the bond-resolved responses, e.g. the change in χ_{ij} , due to a small bond modulation

$$\chi_{ij}^p \equiv - \frac{1}{J_1} \left. \frac{\partial \chi_{ij}}{\partial \kappa} \right|_{\kappa \rightarrow 1} = - \left. \frac{\partial \chi_{ij}}{\partial (\delta J_1)} \right|_{\delta J_1 \rightarrow 0} \quad (4)$$

with J_1 and J_2 fixed. A dramatic enhancement of the χ_{ij}^p around the shaded plaquettes indicates an instability against a small fluctuation of modulation δJ_1 . To compute χ_{ij}^p , we perform two runs of FRG flow with bare couplings $(\kappa J_1 = J_1 + \delta J_1, J_1, J_2)$ and (J_1, J_1, J_2) for a given bond (i, j) . The procedure is expensive but provides invaluable insights.

Phase diagram.—The final results of our FRG calculation are summarized in the phase diagram shown in Fig. 1(b). It contains four phases as J_1/J_2 is varied at fixed $\kappa = 1$. For each phase, a representative value of J_1/J_2 is chosen to illustrate its characteristic FRG flow pattern in two complementary ways. First is the momentum distribution $\tilde{\chi}_r(\mathbf{p})$ near the end of the flow (insets), where the peak momenta are labelled by white ‘x’ in the extended Brillouin zone [40]. Next is the flow of spin susceptibility $\chi(\mathbf{p})$ with the RG scale Λ (main panels) for different channels, i.e., different values of \mathbf{p} . For example, the channel $\mathbf{p} = (\pi, 0)$ is shown in blue, the (π, π) channel in orange, while the flow for the peak momenta labelled by ‘x’ is in red. Clearly, *the leading channels for the four phases are distinct*. Take the case $J_1/J_2 = 1.0$ for example, from the inset it is clear that $\tilde{\chi}_r(\mathbf{p})$ is peaked at $\mathbf{p} = (\pi, \pi)$. Accordingly, the FRG flow for $\chi(\pi, \pi)$ (in orange) is most dominant and

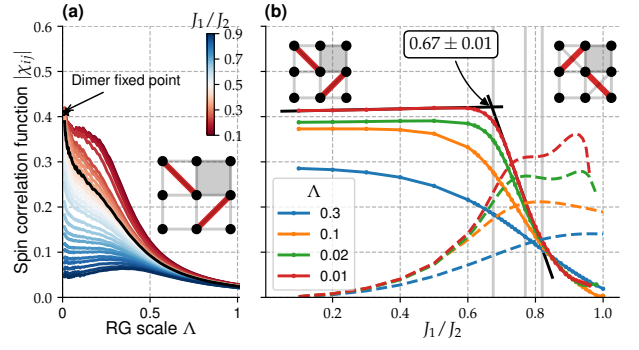


FIG. 2. The dimer and spin liquid phase as the fixed points of the flow of spin-spin correlation functions $\chi_{ij}(\omega \rightarrow 0)$. (a) Flows of χ_{ij} for the dimer bonds (red lines in inset) converge to a constant ≈ 0.41 in the infrared limit for all J_1/J_2 values (color coded, see the colorbar) up until 0.67 indicated by the solid black line. (b) The scale-dependent χ_{ij} (solid lines) for the dimer bonds becomes flat against J_1/J_2 in the infrared limit. Linear regression (black lines) gives the dimer to plaquette transition point $(J_1/J_2)_c = 0.67$. The dashed lines represent χ_{ij} for another set of diagonal bonds (inset at the upper right corner) orthogonal to the dimer bonds. As $\Lambda \rightarrow 0$, it becomes flat for J_1/J_2 between 0.77 and 0.82 where spin liquid is postulated to exist.

rises rapidly as Λ is reduced. The flow breaks down around $\Lambda^* \approx 0.2$, signaling a physical divergence and the onset of magnetic long-range order as seen in many FRG calculations. Thus the Neel phase can be identified unambiguously from the (π, π) peak and the flow divergence.

Outside the Neel phase, the flows appear smooth down to the lowest Λ . This is perhaps not that surprising because spin rotational symmetry is not broken in the dimer or plaquette phase. Yet by inspecting the two cases $J_1/J_2 = 0.3$ and 0.7 in Fig. 1, it is apparent that their spin correlations are rather different, e.g., they have different peak momenta or leading channels. Unfortunately, the information contained in $\chi(\mathbf{p})$ or $\tilde{\chi}_\alpha(\mathbf{p})$ is too crude to differentiate the dimer from the plaquette phase. In what follows, we show that this can be achieved by the FRG flow of bond-resolved spin correlation χ_{ij} .

Dimer phase as a fixed point.—Fig. 2(a) compares the flows of χ_{ij} for the diagonal bond (red lines in the inset) at different values of J_1/J_2 . One notices a remarkable phenomenon: for all $J_1/J_2 < 0.6$, they flow to the same exact value ≈ 0.41 in the infrared $\Lambda \rightarrow 0$. This renormalization group fixed point defines a robust phase with constant spin correlation along the diagonal. This is nothing but the dimer phase, in accordance with the known fact that the ground state wave function in this region is a product state of isolated spin singlets, frozen with respect to J_1/J_2 with constant energy up to a critical point. To determine its phase boundary, Fig. 2(b) plots the diagonal bond correlation in the infrared limit versus J_1/J_2 . It stays completely flat before dropping rapidly in a linear fashion. Linear regression (black lines) yields an intersection point at $J_1/J_2 = 0.67$ which we take as the estimated phase transition point. This critical value is impressively close to 0.675 from large-scale DMRG [3]. The agreement provides strong

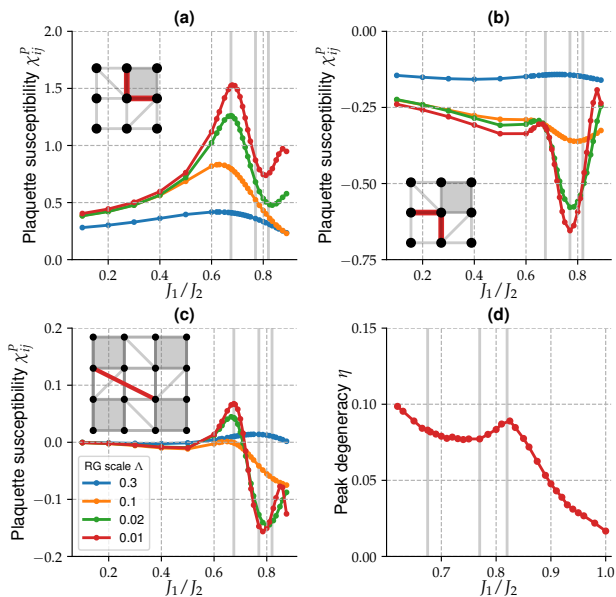


FIG. 3. Identification of the phase boundaries from bond-resolved plaquette susceptibility χ_{ij}^P , which measures the response of a given bond (i, j) [red lines in insets] to a small increase δJ_1 in the shaded squares. (a) A pronounced peak of χ_{\blacksquare}^P around $J_1/J_2 = 0.67$ signals the onset of plaquette order. (b) The suppression dip of χ_{\square}^P at 0.77 indicates the plaquette order is superseded by a new phase, the spin liquid with distinct inter-plaquette correlations. (c) An example of longer range χ_{ij}^P that also develops peak/dip at the two critical points above. (d) The momentum space degeneracy η of $\tilde{\chi}_r(\mathbf{p})$ is peaked at $J_1/J_2 \approx 0.82$, which marks the transition into the Neel phase.

evidence for the validity and accuracy of our FRG calculation.

Plaquette valence bond solid.—Identification of plaquette order from FRG has been an open challenge. In earlier studies, a plaquette susceptibility χ_{PVB} was defined as the propensity towards translational symmetry breaking with respect to a small bond modulation bias [18, 25, 33]. Enhancement of χ_{PVB} has been reported, but to our best knowledge, plaquette order has not been positively identified using pseudofermion FRG so far. For the generalized SS model, we have confirmed that χ_{PVB} is indeed enhanced within a broad region stretching from $J_1/J_2 \sim 0.5$ to 0.7 when compared to its values within the Neel phase (see [39] for details). But it only exhibits a smooth crossover with J_1/J_2 due to the lack of bond resolution. This has motivated us to introduce a more refined measure, the bond-resolved plaquette susceptibility χ_{ij}^P in Eq. (4).

Fig. 3(a) illustrates the χ_{ij}^P for the horizontal/vertical bonds within the slightly strengthened plaquettes (shaded squares), denoted by χ_{\blacksquare}^P . While it is more or less featureless at the ultra-violet scale, as RG steps are taken and Λ is reduced, χ_{\blacksquare}^P gains nontrivial dependence on J_1/J_2 . In particular, in the infrared limit χ_{\blacksquare}^P develops a pronounced peak around $J_1/J_2 \approx 0.67$ [41]. The dramatic enhancement of plaquette susceptibility marks the onset of plaquette order. This independent diagnosis of the dimer-to-plaquette transition agrees very well with the linear regression result above, showing the self-

consistency of our FRG and the advantage of introducing the quantity χ_{ij}^P . It is not a divergence because higher-order vertices are truncated in the current implementation. The onset of plaquette order also manifests in longer range inter-plaquette correlations. Fig. 3(c) depicts the χ_{ij}^P for a bond between an r -site and a b -site from two shaded squares along the lattice diagonal. It too has an enhancement peak at $J_1/J_2 \approx 0.67$.

Further analysis of χ_{ij}^P also points to the demise of the plaquette phase. A pristine plaquette order is adiabatically connected to the limit of decoupled plaquette singlets (shaded squares in Fig. 1 without red or dashed bonds). Upon increasing J_1/J_2 , the plaquette order eventually yields to a state with homogeneous bond energies and very different spin correlations. One possibility is a liquid state where the shaded and empty squares are entangled to feature strong inter-plaquette correlations. The change in correlation is apparent in Fig. 3(c): after the peak, χ_{ij}^P changes sign to develop a sharp dip at $J_1/J_2 \approx 0.78$, suggesting the onset of a new phase. This interpretation is supported by the plaquette susceptibility χ_{\square}^P shown in Fig. 3(b). It measures the change to the bonds around the empty plaquettes in response to $\delta J_1 > 0$ in the nearby shaded squares. When J_1/J_2 is reduced from above toward 0.77, a small δJ_1 leads to significant weakening of the antiferromagnetic bonds (red lines) around the empty squares, i.e. decoupling of the shaded plaquettes to break translational symmetry. Thus the pronounced dip of χ_{\square}^P at $J_1/J_2 \approx 0.77$ [42] marks the upper critical point of the plaquette phase. At the very least, the dramatic variations of χ_{ij}^P are at odds with the scenario that the plaquette phase persists after $J_1/J_2 \approx 0.77$.

A sliver of spin liquid.—The existence of a novel phase after $J_1/J_2 \approx 0.77$ can be inferred independently from the spin correlation χ_{ij} for the diagonal bond shown in Fig. 2(b) (dashed lines). Here it becomes flat, i.e. independent of J_1/J_2 , in the infrared limit. The behavior is distinct from that of a plaquette valence bond solid or a Neel antiferromagnet, for which χ_{ij} increases with J_1 . Since the spin susceptibility flow is continuous down to $\Lambda \rightarrow 0$ as shown in Fig. 1(b), the only plausible scenario seems to be that this FRG fixed point corresponds to a liquid phase. With further increase in J_1 , the flat top of diagonal χ_{ij} is terminated by an upturn around $J_1/J_2 \sim 0.82$, signaling another phase transition. To precisely locate the onset of the Neel order, we adopt an independent criterion [43]. In the postulated spin liquid region, the spin susceptibility $\tilde{\chi}_r(\mathbf{p})$ develops broad maxima, instead of a sharp peak, in momentum space, see the case of $J_1/J_2 = 0.8$ in Fig. 1(b). We can quantify the peak degeneracy by η , the percentage of \mathbf{p} points with $\tilde{\chi}_r(\mathbf{p}) \geq 0.9 \max[\tilde{\chi}_r(\mathbf{p})]$. A similar method was employed in [44] for a different system. The result is shown in Fig. 3(d). As the Neel phase is approached, the broad maxima coalesce into a sharp peak at (π, π) , after which η drops quickly. The peak location of degeneracy η at $J_1/J_2 = 0.82$ serves as an accurate estimation for the transition from the spin liquid to the Neel phase, in excellent agreement with the phase boundary obtained from large scale DMRG [4].

Conclusions.—Our high-resolution FRG analysis of the SS model identifies four phases separated by three critical points

summarized in Fig. 1. Key technical insights are retrieved by monitoring the renormalization group flows of bond-resolved spin-spin correlation functions and susceptibilities. The good agreement with other established numerical methods on the locations of the phase boundaries attests to the accuracy of FRG which takes into account quantum fluctuations in all the channels without bias by tracking millions of effective couplings at each scale Λ . The implementation and analysis strategies reported here can be applied to study other quantum spin Hamiltonians with unconventional magnetic orders using pseudofermion FRG. In particular, our result supports the existence of a finite spin liquid phase rather than a deconfined quantum critical point between the plaquette and Neel phase. It motivates future theoretical work to further elucidate the nature and extent of this phase, and precision measurements to locate and probe spin liquid in $\text{SrCu}_2(\text{BO}_3)_2$.

This work is supported by TUBITAK 2236 Co-funded Brain Circulation Scheme 2 (CoCirculation2) Project No. 120C066 (A.K.) and NSF Grant No. PHY- 2011386 (E.Z.).

* ahmetkeles99@gmail.com

- [1] B. Sriram Shastry and Bill Sutherland, “Exact ground state of a quantum mechanical antiferromagnet,” *Physica B+C* **108**, 1069–1070 (1981).
- [2] Shin Miyahara and Kazuo Ueda, “Theory of the orthogonal dimer Heisenberg spin model for $\text{SrCu}_2(\text{BO}_3)_2$,” *Journal of Physics: Condensed Matter* **15**, R327–R366 (2003).
- [3] Jong Yeon Lee, Yi-Zhuang You, Subir Sachdev, and Ashvin Vishwanath, “Signatures of a Deconfined Phase Transition on the Shastry-Sutherland Lattice: Applications to Quantum Critical $\text{SrCu}_2(\text{BO}_3)_2$,” *Phys. Rev. X* **9**, 041037 (2019).
- [4] Jianwei Yang, Anders W. Sandvik, and Ling Wang, “Quantum Criticality and Spin Liquid Phase in the Shastry-Sutherland model,” (2021), [arXiv:2104.08887 \[cond-mat.str-el\]](https://arxiv.org/abs/2104.08887).
- [5] H. Kageyama, K. Yoshimura, R. Stern, N. V. Mushnikov, K. Onizuka, M. Kato, K. Kosuge, C. P. Slichter, T. Goto, and Y. Ueda, “Exact Dimer Ground State and Quantized Magnetization Plateaus in the Two-Dimensional Spin System $\text{SrCu}_2(\text{BO}_3)_2$,” *Phys. Rev. Lett.* **82**, 3168–3171 (1999).
- [6] Shin Miyahara and Kazuo Ueda, “Exact Dimer Ground State of the Two Dimensional Heisenberg Spin System $\text{SrCu}_2(\text{BO}_3)_2$,” *Phys. Rev. Lett.* **82**, 3701–3704 (1999).
- [7] M. E. Zayed, Ch. Rüegg, A. M. Läuchli, C. Panagopoulos, S. S. Saxena, M. Ellerby, D. F. McMorrow, Th. Strässle, S. Klotz, G. Hamel, *et al.*, “4-spin plaquette singlet state in the Shastry-Sutherland compound $\text{SrCu}_2(\text{BO}_3)_2$,” *Nature physics* **13**, 962–966 (2017).
- [8] Jing Guo, Guangyu Sun, Bowen Zhao, Ling Wang, Wenshan Hong, Vladimir A. Sidorov, Nvsen Ma, Qi Wu, Shiliang Li, Zi Yang Meng, Anders W. Sandvik, and Liling Sun, “Quantum Phases of $\text{SrCu}_2(\text{BO}_3)_2$ from High-Pressure Thermodynamics,” *Phys. Rev. Lett.* **124**, 206602 (2020).
- [9] J. Larrea Jiménez, S. P. G. Crone, E. Fogh, M. E. Zayed, R. Lortz, E. Pomjakushina, K. Conder, A. M. Läuchli, L. Weber, S. Wessel, A. Honecker, B. Normand, Ch. Rüegg, P. Corboz, H. M. Rønnow, and F. Mila, “A quantum magnetic analogue to the critical point of water,” *Nature* **592**, 370–375 (2021).
- [10] Akihisa Koga and Norio Kawakami, “Quantum Phase Transitions in the Shastry-Sutherland Model for $\text{SrCu}_2(\text{BO}_3)_2$,” *Phys. Rev. Lett.* **84**, 4461–4464 (2000).
- [11] Philippe Corboz and Frédéric Mila, “Tensor network study of the Shastry-Sutherland model in zero magnetic field,” *Phys. Rev. B* **87**, 115144 (2013).
- [12] C. Boos, S. P. G. Crone, I. A. Niesen, P. Corboz, K. P. Schmidt, and F. Mila, “Competition between intermediate plaquette phases in $\text{SrCu}_2(\text{BO}_3)_2$ under pressure,” *Phys. Rev. B* **100**, 140413(R) (2019).
- [13] Alexander Wietek, Philippe Corboz, Stefan Wessel, B. Normand, Frédéric Mila, and Andreas Honecker, “Thermodynamic properties of the Shastry-Sutherland model throughout the dimer-product phase,” *Phys. Rev. Research* **1**, 033038 (2019).
- [14] Zhenzhong Shi, Sachith Dissanayake, Philippe Corboz, William Steinhart, David Graf, D. M. Silevitch, Hanna A. Dabkowska, T. F. Rosenbaum, Frédéric Mila, and Sara Haravifard, “Phase diagram of the Shastry-Sutherland Compound $\text{SrCu}_2(\text{BO}_3)_2$ under extreme combined conditions of field and pressure,” (2021), [arXiv:2107.02929 \[cond-mat.str-el\]](https://arxiv.org/abs/2107.02929).
- [15] Joseph Polchinski, “Renormalization and effective Lagrangians,” *Nuclear Physics B* **231**, 269–295 (1984).
- [16] Christof Wetterich, “Exact evolution equation for the effective potential,” *Physics Letters B* **301**, 90–94 (1993).
- [17] Tim R. Morris, “The exact renormalization group and approximate solutions,” *International Journal of Modern Physics A* **09**, 2411–2449 (1994).
- [18] Johannes Reuther and Peter Wölfle, “ J_1 – J_2 frustrated two-dimensional Heisenberg model: Random phase approximation and functional renormalization group,” *Phys. Rev. B* **81**, 144410 (2010).
- [19] Ahmet Keles and Erhai Zhao, “Absence of Long-Range Order in a Triangular Spin System with Dipolar Interactions,” *Phys. Rev. Lett.* **120**, 187202 (2018).
- [20] Ahmet Keles and Erhai Zhao, “Renormalization group analysis of dipolar Heisenberg model on square lattice,” *Phys. Rev. B* **97**, 245105 (2018).
- [21] Andreas Läuchli, Stefan Wessel, and Manfred Sgrist, “Phase diagram of the quadrumerized Shastry-Sutherland model,” *Phys. Rev. B* **66**, 014401 (2002).
- [22] Walter Metzner, Manfred Salmhofer, Carsten Honerkamp, Volker Meden, and Kurt Schönhammer, “Functional renormalization group approach to correlated fermion systems,” *Rev. Mod. Phys.* **84**, 299–352 (2012).
- [23] Peter Kopietz, Lorenz Bartosch, and Florian Schütz, *Introduction to the functional renormalization group*, Lecture Notes in Physics, Vol. 798 (Springer, 2010).
- [24] Finn Lasse Buessen and Simon Trebst, “Competing magnetic orders and spin liquids in two- and three-dimensional kagome systems: Pseudofermion functional renormalization group perspective,” *Phys. Rev. B* **94**, 235138 (2016).
- [25] Yasir Iqbal, Ronny Thomale, F. Parisen Toldin, Stephan Rachel, and Johannes Reuther, “Functional renormalization group for three-dimensional quantum magnetism,” *Phys. Rev. B* **94**, 140408(R) (2016).
- [26] Yasir Iqbal, Pratyay Ghosh, Rajesh Narayanan, Brijesh Kumar, Johannes Reuther, and Ronny Thomale, “Intertwined nematic orders in a frustrated ferromagnet,” *Phys. Rev. B* **94**, 224403 (2016).
- [27] Max Hering and Johannes Reuther, “Functional renormalization group analysis of Dzyaloshinsky-Moriya and Heisenberg spin interactions on the kagome lattice,” *Phys. Rev. B* **95**, 054418 (2017).

- [28] M. L. Baez and J. Reuther, “Numerical treatment of spin systems with unrestricted spin length S : A functional renormalization group study,” *Phys. Rev. B* **96**, 045144 (2017).
- [29] Finn Lasse Buessen, Dietrich Roscher, Sebastian Diehl, and Simon Trebst, “Functional renormalization group approach to $SU(N)$ Heisenberg models: Real-space renormalization group at arbitrary N ,” *Phys. Rev. B* **97**, 064415 (2018).
- [30] Finn Lasse Buessen, Max Hering, Johannes Reuther, and Simon Trebst, “Quantum Spin Liquids in Frustrated Spin-1 Diamond Antiferromagnets,” *Phys. Rev. Lett.* **120**, 057201 (2018).
- [31] Max Hering, Jonas Sonnenschein, Yasir Iqbal, and Johannes Reuther, “Characterization of quantum spin liquids and their spinon band structures via functional renormalization,” *Phys. Rev. B* **99**, 100405(R) (2019).
- [32] Finn Lasse Buessen, Vincent Noculak, Simon Trebst, and Johannes Reuther, “Functional renormalization group for frustrated magnets with nondiagonal spin interactions,” *Phys. Rev. B* **100**, 125164 (2019).
- [33] Yasir Iqbal, Tobias Müller, Pratyay Ghosh, Michel J. P. Gingras, Harald O. Jeschke, Stephan Rachel, Johannes Reuther, and Ronny Thomale, “Quantum and Classical Phases of the Pyrochlore Heisenberg Model with Competing Interactions,” *Phys. Rev. X* **9**, 011005 (2019).
- [34] Finn Lasse Buessen and Yong Baek Kim, “Functional renormalization group study of the Kitaev- Γ model on the honeycomb lattice and emergent incommensurate magnetic correlations,” *Phys. Rev. B* **103**, 184407 (2021).
- [35] Nils Niggemann, Björn Sbierski, and Johannes Reuther, “Frustrated quantum spins at finite temperature: Pseudo-Majorana functional renormalization group approach,” *Phys. Rev. B* **103**, 104431 (2021).
- [36] Dominik Kiese, Tobias Mueller, Yasir Iqbal, Ronny Thomale, and Simon Trebst, “Multiloop functional renormalization group approach to quantum spin systems,” (2021), [arXiv:2011.01269 \[cond-mat.str-el\]](https://arxiv.org/abs/2011.01269).
- [37] Max Hering, Vincent Noculak, Francesco Ferrari, Yasir Iqbal, and Johannes Reuther, “Dimerization tendencies of the pyrochlore Heisenberg antiferromagnet: A functional renormalization group perspective,” (2021), [arXiv:2110.08160 \[cond-mat.str-el\]](https://arxiv.org/abs/2110.08160).
- [38] A. A. Katanin, “Fulfillment of Ward identities in the functional renormalization group approach,” *Phys. Rev. B* **70**, 115109 (2004).
- [39] See Supplemental Material at [URL will be inserted by publisher] for implementation details of Pseudofermion FRG and discussions with additional data which include the additional references [45–47].
- [40] Typically $\chi(\mathbf{p})$ is plotted, which is obtained by summing over $\tilde{\chi}_\alpha$ according to Eq. (3) to obey all crystal symmetries within the Brillouin zone. Here we choose to show $\tilde{\chi}_r$, because it appears less cluttered.
- [41] We have checked that the location of the peak remains the same upon increasing the correlation cutoff R_{max} , adopting a finer frequency grid with lower Δ_{IR} and taking smaller bias δJ_1 .
- [42] We note that the suppression dips in Fig. 3(b) and Fig. 3(c) do not coincide exactly. This discrepancy is expected to reduce with the inclusion of higher order vertices.
- [43] The Neel order is rather weak for $J_1/J_2 < 0.9$, so it is numerically hard to pinpoint at what J_1/J_2 value exactly the divergence sets in. It is more accurate to consider the degeneracy of susceptibility as defined in the main text.
- [44] Yusuke Nomura and Masatoshi Imada, “Dirac-Type Nodal Spin Liquid Revealed by Refined Quantum Many-Body Solver Using Neural-Network Wave Function, Correlation Ratio, and Level Spectroscopy,” *Phys. Rev. X* **11**, 031034 (2021).
- [45] Johannes Reuther, *Frustrated Quantum Heisenberg Antiferromagnets: Functional Renormalization-Group Approach in Auxiliary-Fermion Representation*, Ph.D. thesis (2011).
- [46] Julian Thoenniss, Marc K. Ritter, Fabian B. Kugler, Jan von Delft, and Matthias Punk, “Multiloop pseudofermion functional renormalization for quantum spin systems: Application to the spin- $\frac{1}{2}$ Kagome Heisenberg model,” (2020), [arXiv:2011.01268 \[cond-mat.str-el\]](https://arxiv.org/abs/2011.01268).
- [47] Cornelia Hille, Fabian B. Kugler, Christian J. Eckhardt, Yuan-Yao He, Anna Kauch, Carsten Honerkamp, Alessandro Toschi, and Sabine Andergassen, “Quantitative functional renormalization group description of the two-dimensional Hubbard model,” *Phys. Rev. Research* **2**, 033372 (2020).

Supplementary material for “Rise and fall of plaquette order in Shastry-Sutherland magnet revealed by pseudo-fermion functional renormalization group”

Ahmet Keleş¹ and Erhai Zhao²

¹Department of Physics, Middle East Technical University, Ankara 06800, Turkey

²Department of Physics and Astronomy, George Mason University, Fairfax, Virginia 22030, USA

In the supplementary materials, we give technical details about the implementation of lattice symmetries in the two-particle irreducible vertex. We present a classical phase diagram of generalized Shastry-Sutherland model by taking the static limit of the vertex. We give a detailed scan of the phase diagram and show flow of susceptibilities in the momentum space. We show the plaquette susceptibility flow as defined in the previous FRG studies and further motivate our bond-resolved susceptibility calculations.

1. LATTICE SYMMETRIES IN SHASTRY-SUTHERLAND MODEL

In the Shastry-Sutherland model, there are four lattice sites per unit cell which requires four different sites with colors $\alpha = r, g, b, y$ as reference site. To avoid additional numerical burden stemming from such sublattice symmetries we consider the $\alpha = r$ site at the origin i_0 and consider a cluster of sites with index i_2 within the radius $|\mathbf{r}_{i_0} - \mathbf{r}_{i_2}| < R_{\max}$ independent of sublattice type at i_2 . In the flow equations and susceptibility calculations, whenever we need vertex functions of the form $\Gamma_{ji_2}(s, t, u)$ with a site j of different color $\alpha = g, b, y$, which is not the sublattice type of the central reference site, we use the following lattice symmetry transformations¹

$$\Gamma_{ji_2}(s, t, u) = \Gamma_{i_0j'}(s, t, u) \quad \text{where} \quad j' = \begin{cases} (\delta x, \delta y) & \text{if } j \text{ is } r \\ (\delta y, -\delta x) & \text{if } j \text{ is } g \\ (-\delta x, -\delta y) & \text{if } j \text{ is } b \\ (-\delta y, \delta x) & \text{if } j \text{ is } y \end{cases} \quad (\text{S1})$$

where $(\delta x, \delta y) = \mathbf{r}_{i_2} - \mathbf{r}_j = (x_{i_2} - x_j, y_{i_2} - y_j)$. Furthermore, the vertex functions have the following symmetries

$$\begin{aligned} \Gamma_{i_1i_2}(s, t, u) &\stackrel{s \rightarrow -s, i_1 \leftrightarrow i_2}{=} \Gamma_{i_2i_1}(-s, t, u) \\ &\stackrel{t \rightarrow -t}{=} \Gamma_{i_1i_2}(s, -t, u) \\ &\stackrel{u \rightarrow -u, i_1 \leftrightarrow i_2}{=} \Gamma_{i_2i_1}(s, t, -u) \\ &\stackrel{t \rightarrow -t}{=} \Gamma_{i_1i_2}(u, -t, s) \end{aligned} \quad (\text{S2})$$

which is used to set up a frequency grid only for positive s, t and u which reduces the computational cost significantly. Exchange of the site indices i_1 and i_2 also has to be done in a way to respect the sublattice symmetry. In the vertex $\Gamma_{i_1i_2}$, we assume i_1 is the reference site at the origin, i_2 is a site with coordinates (x, y) then the site flipping operation is done by $\Gamma_{i_1i_2} \rightarrow \Gamma_{i_2i_1} \equiv \Gamma_{i_1,k}$ where k is the index of the site

$$\Gamma_{i_2i_0}(s, t, u) = \Gamma_{i_0i'_2}(s, t, u) \quad \text{where} \quad i'_2 = \begin{cases} (-x, -y) & \text{if } i_2 \text{ is } r \\ (-y, x) & \text{if } i_2 \text{ is } g \\ (x, y) & \text{if } i_2 \text{ is } b \\ (y, -x) & \text{if } i_2 \text{ is } y \end{cases} \quad (\text{S3})$$

for $r_{i_2} = (x, y)$ and $r_{i_0} = (0, 0)$.

Fourier transform with sublattice degrees

$$\chi(\omega, \mathbf{k}) = \frac{1}{4} \sum_{i \in \alpha} \sum_j e^{i\mathbf{k} \cdot (\mathbf{r}_i - \mathbf{r}_j)} \chi_{ij}(\omega) = \frac{1}{4} \left[\chi_r(\omega, k_x, k_y) + \chi_r(\omega, k_y, -k_x) + \chi_r(\omega, -k_x, -k_y) + \chi_r(\omega, -k_y, k_x) \right] \quad (\text{S4})$$

where we defined the susceptibility contribution from the central site in the unit cell

$$\chi_r(\omega, \mathbf{k}) = \sum_j e^{-i\mathbf{k} \cdot \mathbf{r}_j} \chi_{i_0j}(\omega) \quad (\text{S5})$$

and the lattice is setup with $\mathbf{r}_{i_\alpha} = (0, 0)$. The last equality in Eq. S4 can be proven using the symmetry relations given in Eq. S1 and S3.

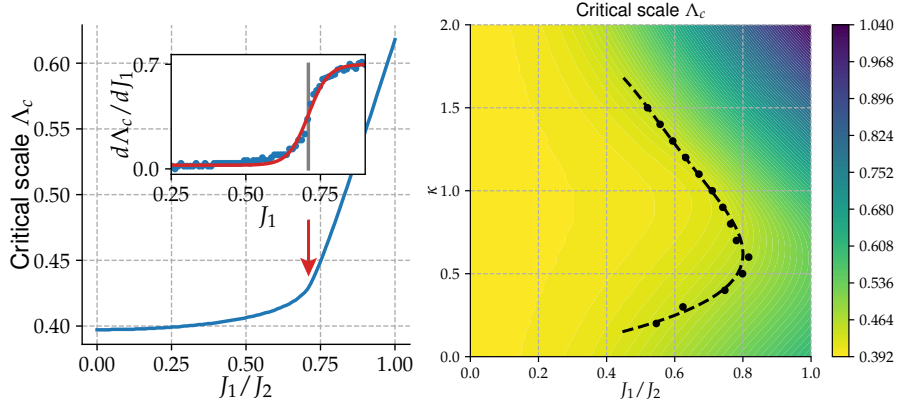


FIG. S1. **Left:** Critical scale of Shastry-Sutherland model obtained from the static limit of FRG equations for a 5×5 lattice. Critical scale is insensitive to J_1 on the left side consistent with decoupled dimers phase and displays a kink around $J_1/J_2 \approx 0.71$ which is found from fitting the derivative to a step-like function, see text for details. This transition point corresponds to the midpoint of the phase transition points 0.675 and 0.77 reported in². On the left side of arrow we found divergence in the $\pi - 0$ channel indicating the dimer phase and on the right we found divergence in $\pi - \pi$ channel indicating the Neel order. **Right:** Critical scale of the quadrumerized Shastry-Sutherland model obtained from static FRG to be compared with the phase diagram in³. Dashed black line is a polynomial fit to the data points of the derivatives $d\Lambda_c/dJ_1$ for different κ shown with filled black circles.

2. STATIC VERTEX LIMIT: CLASSICAL PHASE DIAGRAM

Calculation of the flow equations for frequency independent vertices gives the classical phases of the system and corresponds to Random Phase Approximation (RPA) known in the study of correlated electrons. Here, we include results of our calculation in static limit, which gives a good starting point for understanding the phase diagram.

In the limit of static vertex, self energy vanishes and scale dependent propagator becomes

$$G^\Lambda(\omega) = \frac{\Theta(|\omega| - \Lambda)}{i\omega + i0^+ \text{sign}(\omega)} \quad (\text{S6})$$

where we have added an infinitesimal part in the denominator. Flow equation for the vertex becomes

$$\frac{d}{d\Lambda} \Gamma_{si_1 i_2} = \frac{2}{\pi \Lambda^2} \left[\sum_j \Gamma_{si_1 j} \Gamma_{sj i_2} - 2\Gamma_{si_1 i_2}^2 + \Gamma_{si_1 i_2} \Gamma_{si_1 i_1} \right] \quad (\text{S7})$$

The first term in the susceptibility diagram in the main text can be calculated as

$$\delta_{ij} \text{Tr} \left[\frac{1}{2} \sigma^z \frac{1}{2} \sigma^z \right] \int_{-\infty}^{\infty} \frac{d\omega}{2\pi} G^\Lambda(\omega) G^\Lambda(\omega) = \delta_{ij} \frac{1}{2} \int_{-\infty}^{\infty} \frac{d\omega}{2\pi} \frac{1}{(i\omega + i0^+)^2} = \delta_{ij} \frac{1}{2\pi(\Lambda + 0^+)} \quad (\text{S8})$$

The second term with the static vertex can be calculated similarly giving

$$\chi_{ij}^\Lambda = \frac{1}{2\pi\Lambda} \delta_{ij} - \frac{1}{\pi^2 \Lambda^2} \Gamma_{sij}^\Lambda \quad (\text{S9})$$

In the numerical solution of flow equation Eq. S7 in static limit, vertex functions tend to diverge at small energies signaling the onset of classical long-range orders. In our numerics, when any value in Γ_{ij} reaches a maximum value Γ_{max} , we stop the flow and identify the corresponding scale as the critical scale Λ_c .

The critical scale Λ_c found from static FRG is shown in Fig. S1. For small J_1 , the variation of Λ_c with J_1 is very small. As we approach the phase transition around $J_1 = 0.5$, Λ_c start to deviate from this base value somewhat quadratically and finally it shows linear increase with J_1 inside the known Neel phase. Then, the first derivative of the transition scale Λ_c with respect to J_1 is well approximated with a step-like function. To determine the phase transition point, we calculate the critical scale Λ_c for different values of J_1 and calculate its first derivative $d\Lambda_c/dJ_1$ numerically and fit the result to a function $a + b \tanh[c(x - x_0)]$. The value for x_0 obtained from this fitting with give approximation for the transition point within the static FRG. We determine the kink position $J_c \approx 0.71$, is the midpoint of the two phase transition points reported in the state-of-the-art DRMG simulations. This shows the power of pFRG even in this simplified calculation. Similar calculation for generalized SS model with finite κ is shown in the right panel of Fig. S1.

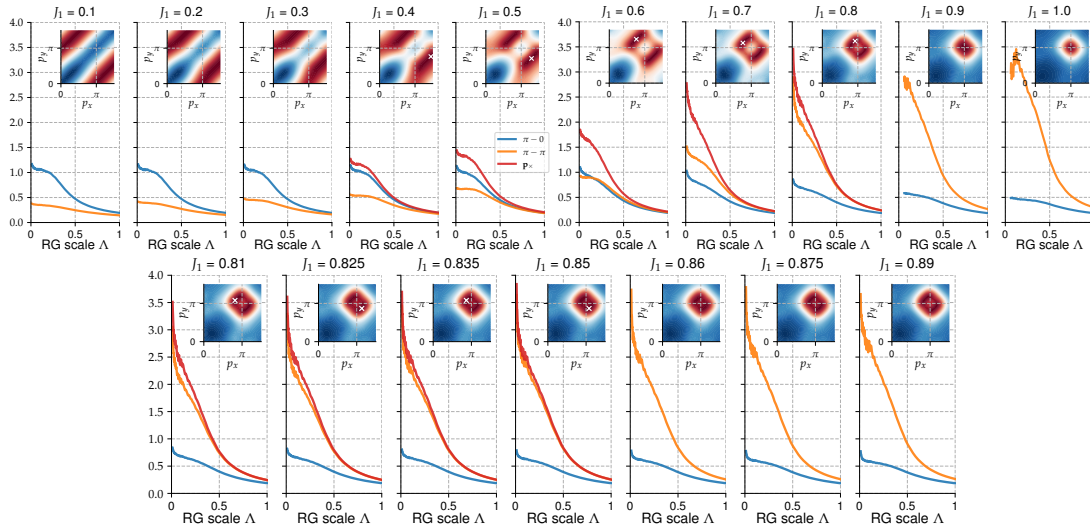


FIG. S2. The susceptibility profiles $\chi(\mathbf{p})$. Main plot shows the flow of maximum susceptibilities and the insets show the susceptibility profiles in the upper right corner of the extended Brillouin zone at a fixed low RG scale $\Lambda = 0.1$ without using the sublattice summations in the Fourier transforms. Lower panels present a denser scan within the small window between plaquette and Neel phases.

3. DETAILED SUSCEPTIBILITY FLOWS IN REAL AND MOMENTUM SPACE

Susceptibility flows in momentum space and real space are shown in Fig. S2 with more data points along the phase diagram.

4. PLAQUETTE SUSCEPTIBILITY WITHOUT BOND RESOLUTION

We probe the plaquette correlations based on the methodology used in the previous pfFRG studies^{4,5} for comparison. We strengthen the couplings between the spins in the shaded plaquette (bond towards upper and right nearest neighbors in Fig. 1 in the main text) $J_1 \rightarrow J_1 + \delta J_1$ and weaken the couplings between the spins in the empty plaquette (lower and left neighbors in Fig.1) $J_1 \rightarrow J_1 - \delta J_1$ in the initial conditions by an infinitesimal amount δJ_1 for fixed $J_2 = 1$ and calculate the following quantity

$$\chi_{PVB} = \frac{J_1 \chi_{ij \in P} - \chi_{ij \notin P}}{\delta J_1 \chi_{ij \in P} + \chi_{ij \notin P}} \quad (\text{S10})$$

where $\chi_{ij \in P}$ and $\chi_{ij \notin P}$ are susceptibilities of the bonds in the strengthened and weakened plaquettes, respectively.

Calculation of this quantity from full FRG is shown in the following Fig. S3. Note that there is no bond resolution in χ_{PVB} . We observe that it increases about five times around $J_1 = 0.6 - 0.7$, which is in the middle of the putative plaquette phase, and goes back down as we approach to Neel phase. In the lower panel, we plot χ_{PVB} along a denser scan of the phase diagram at different RG scales.

χ_{PVB} defined above is able to discern short-ranged plaquette phase from the Neel successfully but it seems to distinguish dimer and plaquette phases only weakly. It can be seen that this susceptibility is significant even for $J_1 < 0.5$, which was shown to be the dimer phase unambiguously in the main text.

5. DEFINITION OF BOND-RESOLVED PLAQUETTE SUSCEPTIBILITY

One can motivate the alternative bond-resolved susceptibility by considering the expression $\langle S_i S_j \rangle = \text{Tr}(S_i \cdot S_j e^{-\beta H}) / \text{Tr}(e^{-\beta H})$ and taking the derivative of both sides with respect to J_{kl} (coupling between spins S_k and S_l) in a way that i, j, k, l are corners of a given plaquette pattern while keeping all other couplings fixed. It is easy to show $\partial \chi_{ij} / \partial J_{kl} = -\beta \langle (S_i \cdot S_j)(S_k \cdot S_l) \rangle + \beta \langle S_i \cdot S_j \rangle \langle S_k \cdot S_l \rangle$ which is the connected average of the four spin operators at sites i, j, k and l .

To calculate this equation in practice, we start with Shastry-Sutherland model for a given nearest-neighbors coupling J_1 by taking $J_2 = 1$, we calculate the susceptibility $\chi_{ij}[J_1]$ as usual; we increase the strength of exchange coupling $J_1 \rightarrow J_1 + \delta J_1$ only for the target plaquette (upper neighbor and right neighbor couplings $J_1 + \delta J_1$ but lower neighbor and left neighbor couplings

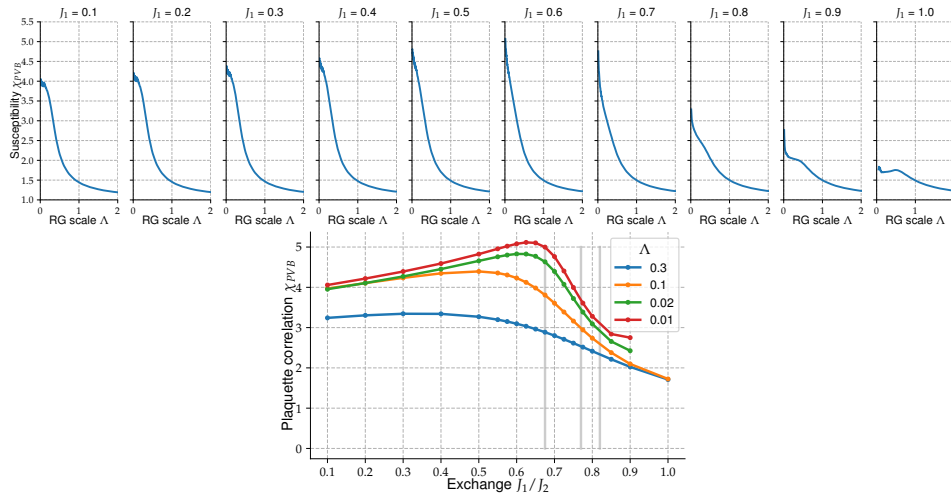


FIG. S3. Plaquette susceptibility without bond resolution. Upper panels show the flow of susceptibility χ_{PVB} for selected points along the phase diagram. Lower panel shows the denser scan of χ_{PVB} for three different low RG scales.

are still J_1) and calculate the resulting susceptibility $\chi_{ij}[J_1 + \delta J_1]$; finally define the following correlation function

$$\chi_{ij}^P \equiv \frac{\chi_{ij}[J_1 + \delta J_1] - \chi_{ij}[J_1]}{\delta J_1}. \quad (\text{S11})$$

This procedure requires running numerically expensive pfFRG simulation for two points that are infinitesimally close to each other in the phase diagram but it provides a useful perspective.

6. HIGHER-LOOP CONTRIBUTIONS

In this section, we discuss the limitation of our calculation and the possible extension of our work to include higher-loop contributions. To solve the formally exact flow equations, most FRG implementations involve two numerical aspects, both of which influence the accuracy and the computational cost of the algorithm. First is the truncation of the infinite hierarchy of flow equations to a certain loop order plus higher order correction terms. In the context of pseudo-fermion FRG, the one-loop truncation plus the Katanin terms as implemented here has been extensively applied and benchmarked. For interacting system, no numerical implementation of FRG manages to include all diagrams to infinite loop order. Empirically, most known divergences (instabilities toward long-range order), and the mutual influence of these instabilities, seem to be accounted already at the level of one-loop diagrams for interacting fermions. Second is the resolution for momentum and frequency in the numerical solution of the truncated flow equations. The term “high-resolution” throughout our manuscript refers to the frequency as well as the momentum resolution (or equivalently, the site resolution, which in our implementation is determined by the cut-off correlation length in real space). A main technical effort of our work is to achieve sufficient frequency and site resolution, which as we have seen in the main text is crucial to analyze the plaquette susceptibility, leading to the identification of an unexpected spin liquid region. For example, with 64 grid points in the frequency and $21 \times 21 = 441$ lattice sites, we end up with 120 million running couplings. Decreasing the frequency resolution from 64 to 48 decreases to the number of coupling to about 50 million but the change in the flow of spin susceptibilities are almost the same at the level of machine precision. The computation is made feasible by migrating to GPU. The improved resolution not only can help identify complex long-range orders hitherto impossible, but also can provide fresh physical insight by comparing the various bond-resolved susceptibilities.

A natural question is then “how important are additional higher loop contributions?” A definitive answer to this questions would require solving the flow equation with additional higher-loop terms systematically taken into account, which is beyond the computing resources available to us at the moment. But in principle, bond-resolved spin and plaquette susceptibilities can be calculated with additional higher-loop contributions. This would be the subject of a future research.

Very recently, a few groups have begun to shed light on this open question by explicitly taking into account additional higher-loop contributions^{6,7}. In assessing these results and discussing higher-loop expansions, one must carefully distinguish FRG for itinerant fermions and pf-fRG for quantum spin systems, because the nature of the loop expansion, hence the role played by the higher loops are drastically different. For itinerant fermions, such as the one-band Fermi-Hubbard model on square lattice studied by Hille et al.⁸, one motivation to include higher loop contributions is to accurately describe the momentum and frequency dependence of the self-energy, which was neglected in many of the earlier N-patch FRG studies. The other motivation

is to achieve quantitative agreement with Parquet approximation and Determinant quantum Monte Carlo. It remains to be seen how such “improved fRG*” performs when away from half-filling.

For quantum spin systems, two recent works investigated the higher-loop corrections in pf-fRG^{6,7}. As we outlined in the main text, the pseudo-fermion representation of spin models leads to a strongly interacting system where the bare kinetic energy is zero. Here the loop expansion is motivated more by the spirit of $1/S$ or $1/N$ expansion^{9,10}. (In pseudo-fermion FRG, the frequency dependence of self-energy plays a crucial role and is already taken into account from the very beginning.) To our knowledge, there still lacks a satisfactory understanding of the role of higher-loop contributions, including its convergence properties when long-range or spin liquid phases are approached in the infrared limit. The state-of-the-art multiple-loop pf-fRG seems to imply that the divergence towards long-range order, or the lack thereof, is dictated by the leading contributions contained in the level-one truncation (one loop plus Katanin terms, as implemented in our work). Moreover, our confidence in the performance of pf-fRG applied to the Shastry-Sutherland (SS) model stems from its (unexpected) remarkable agreement with other independent, state-of-the-art methods such as DRMG regarding the phase boundaries. Future work will elucidate whether or how the predicted phase boundary may change with higher order contributions included in a consistent manner.

-
- ¹ Johannes Reuther, *Frustrated Quantum Heisenberg Antiferromagnets: Functional Renormalization-Group Approach in Auxiliary-Fermion Representation*, Ph.D. thesis (2011).
- ² Jong Yeon Lee, Yi-Zhuang You, Subir Sachdev, and Ashvin Vishwanath, “Signatures of a Deconfined Phase Transition on the Shastry-Sutherland Lattice: Applications to Quantum Critical $\text{SrCu}_2(\text{BO}_3)_2$,” *Phys. Rev. X* **9**, 041037 (2019).
- ³ Andreas Läuchli, Stefan Wessel, and Manfred Sigrist, “Phase diagram of the quadrumerized Shastry-Sutherland model,” *Phys. Rev. B* **66**, 014401 (2002).
- ⁴ Johannes Reuther and Peter Wölfle, “ J_1 – J_2 frustrated two-dimensional Heisenberg model: Random phase approximation and functional renormalization group,” *Phys. Rev. B* **81**, 144410 (2010).
- ⁵ Yasir Iqbal, Tobias Müller, Pratyay Ghosh, Michel J. P. Gingras, Harald O. Jeschke, Stephan Rachel, Johannes Reuther, and Ronny Thomale, “Quantum and Classical Phases of the Pyrochlore Heisenberg Model with Competing Interactions,” *Phys. Rev. X* **9**, 011005 (2019).
- ⁶ Dominik Kiese, Tobias Mueller, Yasir Iqbal, Ronny Thomale, and Simon Trebst, “Multiloop functional renormalization group approach to quantum spin systems,” (2021), [arXiv:2011.01269 \[cond-mat.str-el\]](https://arxiv.org/abs/2011.01269).
- ⁷ Julian Thoenniss, Marc K. Ritter, Fabian B. Kugler, Jan von Delft, and Matthias Punk, “Multiloop pseudofermion functional renormalization for quantum spin systems: Application to the spin- $\frac{1}{2}$ kagome Heisenberg model,” (2020), [arXiv:2011.01268 \[cond-mat.str-el\]](https://arxiv.org/abs/2011.01268).
- ⁸ Cornelia Hille, Fabian B. Kugler, Christian J. Eckhardt, Yuan-Yao He, Anna Kauch, Carsten Honerkamp, Alessandro Toschi, and Sabine Andergassen, “Quantitative functional renormalization group description of the two-dimensional hubbard model,” *Phys. Rev. Research* **2**, 033372 (2020).
- ⁹ M. L. Baez and J. Reuther, “Numerical treatment of spin systems with unrestricted spin length S : A functional renormalization group study,” *Phys. Rev. B* **96**, 045144 (2017).
- ¹⁰ Finn Lasse Buessen, Dietrich Roscher, Sebastian Diehl, and Simon Trebst, “Functional renormalization group approach to $SU(N)$ Heisenberg models: Real-space renormalization group at arbitrary N ,” *Phys. Rev. B* **97**, 064415 (2018).